Enhancing electrochemical intermediate solvation through electrolyte anion selection to increase nonaqueous Li-O_2 battery capacity

Supplemental Information

Colin M. Burke[1,2], Vikram Pande[3], Abhishek Khetan[4], Venkatasubramanian Viswanathan[3]* and Bryan D. McCloskey[1,2]*

[1]*Department of Chemical and Biomolecular Engineering, University of California, Berkeley, CA, 94720*
[2]*Environmental Energy Technologies Division, Lawrence Berkeley National Laboratory, Berkeley, CA, 94720*
[3]*Department of Mechanical Engineering, Carnegie Mellon University, Pittsburgh, PA, 15213*
[4]*Institute for Combustion Technology, Rheinisch-Westfälische Technische Hochschule, Aachen 52056, Germany*

*bmcclosk@berkeley.edu, venkvis@cmu.edu

Materials. Lithium nitrate (BioUltra) and lithium bromide (ReagentPlus) were purchased from Sigma Aldrich and were dried under vacuum in a heated glove box antechamber at 150°C for 24 hours before use. Lithium bis(trifluoromethane) sulfonimide (LiTFSI), 1,2-dimethoxyethane, and dimethyl sulfoxide were purchased from BASF and used as received. Whatman QM-A glass fiber filters were purchased from VWR. PTFE (60 wt% dispersion in H_2O) was purchased from Sigma Aldrich. Vulcan XC72 was purchased from Fuel Cell Store and was filtered through a 60 mesh screen. T316 stainless steel 120 mesh, with wire diameter 0.0026", was purchased from TWP Inc. Research-grade oxygen and argon were purchased from Praxair. 99% $^{18}O_2$ was purchased from Sigma Aldrich. All electrolyte, cell, and NMR sample preparation was completed in an argon-filled glove box with <0.1ppm O_2 and <0.1ppm H_2O.

In preparing the electrolytes, we found the solubility limit of $LiNO_3$ in DME is approximately 1M. The capacity variability of the 0.7M $LiNO_3$ cell in Figure 1 is likely due to concentration polarization effects in the electrolyte, as 0.7M begins to approach the solubility limit of $LiNO_3$ in DME, such that $LiNO_3$ precipitation at the anode may occur. The $LiNO_3$ concentration range (<0.7M) we report was limited by this effect.

Cathode preparation. Cathodes were prepared via a similar method to that described previously.(1) A mixture of 3:1 w:w ratio of Vulcan XC72 to PTFE binder in IPA and water (4:1 water:IPA; and 15mL total for 400mg C) was sonicated for 30

seconds and homogenized for 6 minutes. A Badger model 250 air-sprayer was used to spray the slurry onto a piece of stainless steel mesh roughly 4.5" square, which had been rinsed with IPA and acetone and dried at 150°C for ten minutes prior to use. After letting the spray-coated mesh air-dry, 12mm diameter cathodes were punched out, rinsed with IPA and acetone, and dried at 150°C under vacuum for at least 12 hours. The cathodes were then transferred, while hot, into the glove box, and stored on a hot plate at 200°C.

Carbon loading. Cell capacities depend on carbon loading. To keep carbon loading consistent, the cathodes used for any particular data set, such as the capacity measurements displayed in Figure 1 or the cathode morphology images in Figure 2, were all from the same batch of spray-coated cathodes. As a control, the capacity measurements presented in Figure 1 were repeated with a second batch of cathodes. All capacities changed proportionally (a slight increase for all cases), with the capacity of the cell using 0.5M $LiNO_3$:0.5M LiTFSI in DME maintaining just over a three-fold increase from the capacity of the cell employing 1M LiTFSI in DME. Cathodes contained on average 1.5-2.0 mg/cm^2 carbon.

Cell preparation. The Li-O_2 cells used throughout this paper followed the same Swagelok design as described previously.(2) All cells employed a 7/16" diameter lithium foil, a 1/2" diameter Whatman QM-A glass fiber separator, a 12mm diameter cathode of Vulcan XC72 carbon on stainless steel mesh, and a 1mm thick, 1/2" diameter stainless steel ring. The QM-A separators, like the cathodes, were rinsed with IPA and acetone and dried under vacuum at 150°C under vacuum for at least 12 hours before being transferred to the glove box and stored on a hot plate at 200°C. Each battery contained 80 μL of electrolyte.

Scanning electron microscopy. Discharged cathodes were characterized via scanning electron microscopy immediately after discharge. After replacing discharged cells' headspaces with argon, the cells were transferred into the glove box, and the cathodes were removed. The cathodes were each rinsed with two 1 mL aliquots of DME and were subsequently dried under vacuum for at least five minutes in the glove box antechamber. The cathodes were then sealed in septa vials,

removed from the glove box, and taken to the SEM. Immediately before imaging, the cathodes were removed from the argon-filled septa vials, placed on carbon tape on the SEM holder, and inserted into the SEM. From discharge completion to SEM insertion was typically one hour. From removing the cathodes from the septa vials to SEM insertion was typically less than 30 seconds. SEM was performed on a JEOL JSM-7500f.

Titration. The Li_2O_2 titration protocol used here followed that described previously.(1) After replacing the discharged cells' headspaces with argon, the cells were transferred into the glove box, and the cathodes were removed. Each cathode was placed in a 20mL septa vial. The cathodes were placed under vacuum for at least three minutes to evaporate any residual solvent before the vial caps were tightly sealed and the vials were removed from the glove box. 2mL of ultrapure water (18.2MΩ cm, Millipore) was injected through the septa to react the Li_2O_2 into LiOH and H_2O_2. LiOH was quantified by using phenolphthalein as an indicator and HCl as a titrant. H_2O_2 was quantified via an iodometric titration employing potassium iodide, sulfuric acid, and a molybdate catalyst solution to create I_2 and sodium thiosulfate as a titrant for the I_2. Starch was used to sharpen the end point, which turned from dark blue to clear at the end of the titration. The Li_2O_2 percent yield is defined as the amount of Li_2O_2 formed during discharge, as quantified via an iodometric titration, to the amount of Li_2O_2 expected from coulometry, assuming an ideal $2e^-/Li_2O_2$ process.(1) Of note, no titratable I_2 was observed from titrations on the separator alone, confirming the following two points: a) no NO_2^- that may have formed at the Li metal anode is present in the separator, and therefore NO_2^- does not result in a falsely higher Li_2O_2 yield as measured using the iodometric titration (NO_2^- also oxidizes I^-); b) Li_2O_2 only forms on the cathode and not the separator.

Nuclear Magnetic Resonance Spectroscopy. ^7Li and ^{23}Na nuclear magnetic resonance spectroscopy measurements were completed on a Bruker AM-400 magnet with a 5mm Z-gradient broad brand probe. Reference samples, those employing a chloride salt in D_2O, were prepared outside the glove box and were flame-sealed in melting point capillaries. Electrolyte samples were prepared inside the glove box and were placed, along with a reference capillary, in a Wilmad screw-

cap NMR tube. All reference samples were 3M of the chloride salt in D_2O. For the ^{23}Na NMR, 0.2M $NaClO_4$ was added. These molarities were taken from Schmeisser et al.(3) ^{23}Na NMR spectra are not reported here because of the poor solubility of $NaNO_3$ in DME. NMR spectra of only the reference and only the sample were taken to verify the identity of each peak. A representative ^{7}Li NMR spectrum of a 0.5M LiTFSI:0.5M $LiNO_3$ in DME electrolyte is shown in Figure S7.

Water controls. With the solubility mechanism confirmed, it was important to check that the increased solubility was indeed due to DN effects of NO_3^- and not another experimental artifact, in particular water contamination. As a first control, the key experiments were repeated with new electrolyte solutions that used lithium nitrate powder that had been dried a second time under vacuum in a heated glove box antechamber at 150°C for 24 hours. All repeated experiments gave consistent results with their original counterparts. As a second control, water levels in the electrolytes were measured via Karl Fischer titration. All electrolytes had less than 70ppm water, although the 1M LiTFSI (0M $LiNO_3$) and LiBr-containing electrolytes had <10ppm water content. Therefore, a battery employing an electrolyte of 1M LiTFSI in DME with 70ppm of water was discharged at 450 $\mu A/cm^2$ to 2V, analogous to the batteries in Figure 1. As observed in Figure S13, this battery saw an increase in capacity of 40% compared to a battery with 1M LiTFSI in DME, much smaller than the four-fold increase displayed in Figure 1 from the cell employing the 0.3M LiTFSI:0.7M $LiNO_3$ electrolyte.

Ising Model for Li^+ solvation shell. The Ising model is a mathematical method of using discrete variables, usually called spin, on a graph or lattice to represent interactions in a system. In its most general form, the model allows for the identification of phase transitions in systems exhibiting magnetism, specific adsorption, etc. Although the model is exactly solvable only up to 2 dimensions, problems in higher dimensions can be addressed by modifying the model using concepts from mean field theory.

In order to find the composition and solvation energetics in the first solvation shell of Li^+ ions, we apply the Ising model within the mean-field approximation. We assume the first solvation shell to be comprised of either the

solvent molecules or the salt anions, which interact with the Li^+ ion and also with each other due to their electron donating/accepting tendency. Owing to their extremely low concentration in the solution phase, we neglect the effect of O_2^- anions in the Li^+ solvation shell. Additionally, O_2^- anions have an incomplete shell configuration and are not known to be keen donors of electrons.

The solvation shell of an ion is an interacting system i.e. interactions between different molecules in the solvation shell affects their occupancy in the solvation shell. A solvation shell can be considered as a spherical lattice because it is spatially invariant with respect to Li^+. The Hamiltonian, which describes the total energy of interactions involved in the solvation shell, is constructed by summing over all the interaction energies and the energies associated with a particular species occupying a site in the solvation shell. To describe the occupation of different species in the solvation shell at a given site i, we use the occupation (spin) variables given as species $\sigma_i = \{l, m, n\}$, for each kind of species. The occupation variables 'n', 'm' and 'l' represent the occupancy of a site by the solvent, the NO_3^- anions and the $TFSI^-$ anions respectively. For any site 'i' occupied by the solvent, the occupation variables will have the value $n_i = 1$, $m_i = 0$ and $l_i = 0$ and so on. Thus at any given site, we have $n_i + m_i + l_i = 1$.

The key energetic contributions for each of the species are dependent on the kind interaction they have with the Li^+ cation, with other molecules in the solvation shell and the entropy loss associated with the species being configurationally pinned in the solvation shell as compared to its mobile state in the bulk. We limit the expansion of the Ising model to nearest neighbor interactions in the imagined spherical lattice that comprises the first solvation shell because only these interactions have a dominant contribution to the total energy. The energetic interactions in the solvation shell of Li^+ can thus be described by a model Hamiltonian, H, given by:

$$H = h_1 \sum_{i=1}^{N} n_i + h_2 \sum_{i=1}^{N} m_i + h_3 \sum_{i=1}^{N} l_i + J_{11} \sum_{\langle i,j \rangle} n_i n_j + J_{22} \sum_{\langle i,j \rangle} m_i m_j + J_{33} \sum_{\langle i,j \rangle} l_i l_j$$
$$J_{12} \sum_{\langle i,j \rangle} n_i m_j + J_{21} \sum_{\langle i,j \rangle} m_i n_j + J_{13} \sum_{\langle i,j \rangle} n_i l_j + J_{31} \sum_{\langle i,j \rangle} l_i n_j + J_{23} \sum_{\langle i,j \rangle} m_i l_j + J_{32} \sum_{\langle i,j \rangle} l_i m_j \quad \text{(S1)}$$

In our model, h_1 represents the interaction energy between a Li^+ ion and a solvent, h_2 represents the interaction energy between a NO_3^- anion and Li^+ and h_3 represents the interaction energy between a $TFSI^-$ anion and Li^+ .The coupling constant J_{11} represents the interaction between neighboring solvent molecules in the Li^+ solvation shell. Likewise J_{22} and J_{33} represent the interaction between neighboring NO_3^- and neighbouring $TFSI^-$ anions respectively. Owing to symmetry, $J_{12} = J_{21}$, $J_{13} = J_{31}$, $J_{23} = J_{32}$. The cross-coupling terms, J_{12}, J_{13} and J_{23}, represent interactions between neighboring NO_3^- and solvent molecules, neighboring $TFSI^-$ and solvent molecules and neighboring $TFSI^-$ and NO_3^- anions, respectively.

The Ising model developed here is modified within the framework of a mean field approximation in order to make it solvable, and thus determine the composition of the solvation shell and also the free energy of solvation of Li^+ cation. In the mean field approximation the nearest neighbor interaction terms of the kind $\{\sigma_i\sigma_j\}$ between two species at sites i and j can be replaced by the average interaction $\{\sigma_i\langle\sigma\rangle\}$ where $\langle\sigma\rangle$ stands for the average occupation for the species in the shell and is defined as $\langle\sigma\rangle = \frac{1}{N}\sum_{i=1}^{N}\langle\sigma_i\rangle$. It is important to note that this quantity is spatially invariant, $\langle\sigma\rangle = \langle\sigma_i\rangle$ which implies $J_{ij}\sum_{\langle i,j\rangle}\sigma_i\sigma_j \approx J_{ij}z\,\langle\sigma\rangle\sum_i\sigma_i$, where z is the coordination number. For the small sized Li^+ cation, we assume that the first solvation shell has N = 4 sites and hence the coordination number z = N/2 = 2 (to avoid double counting). We assume that z is independent of the occupying species in the solvation shell.

Hence, the Hamiltonian, H, under the mean-field approximation is then given by:

$$\begin{aligned} H = {} & h_1\sum_{i=1}^{N} n_i + h_2\sum_{i=1}^{N} m_i + h_3\sum_{i=1}^{N} l_i + J_{11}z\langle n\rangle\sum_{i=1}^{N} n_i + J_{22}z\langle m\rangle\sum_{i=1}^{N} m_i + J_{33}z\langle l\rangle\sum_{i=1}^{N} l_i \\ & + J_{12}\frac{z}{2}\langle m\rangle\sum_{i=1}^{N} n_i + J_{21}\frac{z}{2}\langle n\rangle\sum_{i=1}^{N} m_i + J_{13}\frac{z}{2}\langle l\rangle\sum_{i=1}^{N} n_i + J_{31}\frac{z}{2}\langle n\rangle\sum_{i=1}^{N} l_i \\ & + J_{23}\frac{z}{2}\langle l\rangle\sum_{i=1}^{N} m_i + J_{32}\frac{z}{2}\langle m\rangle\sum_{i=1}^{N} l_i \qquad (S2) \end{aligned}$$

The average occupation for a given species at any site in the solvation sphere can be found by performing an average on each occupation variable using the mean field site energy in the Boltzmann weights as its probabilities, given by:

$$\langle \mathrm{n} \rangle = \frac{\sum_{\mathrm{n}=0,1} \sum_{\mathrm{m}=0,1} \sum_{\mathrm{l}=0,1} \mathrm{n} \exp\left(\frac{-\mathrm{H}}{\mathrm{kT}}\right)}{\sum_{\mathrm{n}=0,1} \sum_{\mathrm{m}=0,1} \sum_{\mathrm{l}=0,1} \exp\left(\frac{-\mathrm{H}}{\mathrm{kT}}\right)} \qquad (S3.a)$$

$$\langle \mathrm{m} \rangle = \frac{\sum_{\mathrm{n}=0,1} \sum_{\mathrm{m}=0,1} \sum_{\mathrm{l}=0,1} \mathrm{m} \exp\left(\frac{-\mathrm{H}}{\mathrm{k}T}\right)}{\sum_{\mathrm{n}=0,1} \sum_{\mathrm{m}=0,1} \sum_{\mathrm{l}=0,1} \exp\left(\frac{-\mathrm{H}}{\mathrm{kT}}\right)} \qquad (S3.b)$$

$$\langle \mathrm{l} \rangle = \frac{\sum_{\mathrm{n}=0,1} \sum_{\mathrm{m}=0,1} \sum_{\mathrm{l}=0,1} \mathrm{l} \exp\left(\frac{-\mathrm{H}}{\mathrm{kT}}\right)}{\sum_{\mathrm{n}=0,1} \sum_{\mathrm{m}=0,1} \sum_{\mathrm{l}=0,1} \exp\left(\frac{-\mathrm{H}}{\mathrm{kT}}\right)} \qquad (S3.c)$$

On expanding these expressions, we get the average occupation of solvent and salt anions at a site in the Li^+ solvation shell as given below:

$$\langle \mathrm{n} \rangle = \frac{\exp\left(\frac{\left(-\mathrm{h}_1 - \mathrm{J}_{11}\mathrm{z}\langle \mathrm{n} \rangle - \mathrm{J}_{12}\frac{\mathrm{z}}{2}\langle \mathrm{m} \rangle - \mathrm{J}_{13}\frac{\mathrm{z}}{2}\langle \mathrm{l} \rangle\right)}{\mathrm{kT}}\right)}{\exp\left(\frac{\left(-\mathrm{h}_1 - \mathrm{J}_{11}\mathrm{z}\langle \mathrm{n} \rangle - \mathrm{J}_{12}\frac{\mathrm{z}}{2}\langle \mathrm{m} \rangle - \mathrm{J}_{13}\frac{\mathrm{z}}{2}\langle \mathrm{l} \rangle\right)}{\mathrm{kT}}\right) + \exp\left(\frac{\left(-\mathrm{h}_2 - \mathrm{J}_{22}\mathrm{z}\langle \mathrm{m} \rangle - \mathrm{J}_{21}\frac{\mathrm{z}}{2}\langle \mathrm{n} \rangle - \mathrm{J}_{23}\frac{\mathrm{z}}{2}\langle \mathrm{l} \rangle\right)}{\mathrm{kT}}\right) + \exp\left(\frac{\left(-\mathrm{h}_3 - \mathrm{J}_{33}\mathrm{z}\langle \mathrm{l} \rangle - \mathrm{J}_{31}\frac{\mathrm{z}}{2}\langle \mathrm{n} \rangle - \mathrm{J}_{32}\frac{\mathrm{z}}{2}\langle \mathrm{m} \rangle\right)}{\mathrm{kT}}\right)} \qquad (S4.a)$$

$$\langle \mathrm{m} \rangle = \frac{\exp\left(\frac{\left(-\mathrm{h}_2 - \mathrm{J}_{22}\mathrm{z}\langle \mathrm{m} \rangle - \mathrm{J}_{21}\frac{\mathrm{z}}{2}\langle \mathrm{n} \rangle - \mathrm{J}_{23}\frac{\mathrm{z}}{2}\langle \mathrm{l} \rangle\right)}{\mathrm{kT}}\right)}{\exp\left(\frac{\left(-\mathrm{h}_1 - \mathrm{J}_{11}\mathrm{z}\langle \mathrm{n} \rangle - \mathrm{J}_{12}\frac{\mathrm{z}}{2}\langle \mathrm{m} \rangle - \mathrm{J}_{13}\frac{\mathrm{z}}{2}\langle \mathrm{l} \rangle\right)}{\mathrm{kT}}\right) + \exp\left(\frac{\left(-\mathrm{h}_2 - \mathrm{J}_{22}\mathrm{z}\langle \mathrm{m} \rangle - \mathrm{J}_{21}\frac{\mathrm{z}}{2}\langle \mathrm{n} \rangle - \mathrm{J}_{23}\frac{\mathrm{z}}{2}\langle \mathrm{l} \rangle\right)}{\mathrm{kT}}\right) + \exp\left(\frac{\left(-\mathrm{h}_3 - \mathrm{J}_{33}\mathrm{z}\langle \mathrm{l} \rangle - \mathrm{J}_{31}\frac{\mathrm{z}}{2}\langle \mathrm{n} \rangle - \mathrm{J}_{32}\frac{\mathrm{z}}{2}\langle \mathrm{m} \rangle\right)}{\mathrm{kT}}\right)} \qquad (S4.b)$$

$$\langle \mathrm{l} \rangle = \frac{\exp\left(\frac{\left(-\mathrm{h}_3 - \mathrm{J}_{33}\mathrm{z}\langle \mathrm{l} \rangle - \mathrm{J}_{31}\frac{\mathrm{z}}{2}\langle \mathrm{n} \rangle - \mathrm{J}_{32}\frac{\mathrm{z}}{2}\langle \mathrm{m} \rangle\right)}{\mathrm{kT}}\right)}{\exp\left(\frac{\left(-\mathrm{h}_1 - \mathrm{J}_{11}\mathrm{z}\langle \mathrm{n} \rangle - \mathrm{J}_{12}\frac{\mathrm{z}}{2}\langle \mathrm{m} \rangle - \mathrm{J}_{13}\frac{\mathrm{z}}{2}\langle \mathrm{l} \rangle\right)}{\mathrm{kT}}\right) + \exp\left(\frac{\left(-\mathrm{h}_2 - \mathrm{J}_{22}\mathrm{z}\langle \mathrm{m} \rangle - \mathrm{J}_{21}\frac{\mathrm{z}}{2}\langle \mathrm{n} \rangle - \mathrm{J}_{23}\frac{\mathrm{z}}{2}\langle \mathrm{l} \rangle\right)}{\mathrm{kT}}\right) + \exp\left(\frac{\left(-\mathrm{h}_3 - \mathrm{J}_{33}\mathrm{z}\langle \mathrm{l} \rangle - \mathrm{J}_{31}\frac{\mathrm{z}}{2}\langle \mathrm{n} \rangle - \mathrm{J}_{32}\frac{\mathrm{z}}{2}\langle \mathrm{m} \rangle\right)}{\mathrm{kT}}\right)} \qquad (S4.c)$$

Finally, to obtain the values for average occupation, we need to ascribe the appropriate mathematical functions for all of the energetic interaction terms. The interaction term h_1 is dependent on the donating tendency of the solvent molecule

to the Li^+ ions in solution. This can be attributed to the free energy of Li^+ ions in a particular solvent. The free energy of Li^+ ions in solvent HA can be determined from the equilibrium between solvated Li^+ ions and metallic Li in a solvent HA, given by

$$Li_{(s)} \rightleftharpoons Li^+_{HA} + e^- \quad (S5)$$

The free energy of Li^+ ions, $G_{Li^+_{HA}}$, can thus be expressed in terms of the half wave potential of Li/Li^+ couple in that solvent, U_{Li/Li^+}, and the free energy of metallic lithium, $G_{Li_{(s)}}$, as:

$$G_{Li^+_{HA}} = G_{Li_{(s)}} + eU_{Li/Li^+} \quad (S6)$$

It has been shown experimentally that the half wave potential of Li/Li^+ redox couple varies with the DN of the solvent.(4) As described in our previous work,(5) the free energy of the Li^+ ion, and thus the interaction term h_1 between solvent HA and Li^+ , can be given as $h_1 = 0.001844\, DN_{HA}^2 - 0.11314\, DN_{HA}$. While similar experiments have not been performed for anions, we expect a similar relationship to hold for the interaction terms h_2 and h_3 between the Li^+ cation and the anions, given that the DN of the anions are measured on a scale similar to that of the solvents. Thus, the interaction terms of the anions with Li^+ (h_2 and h_3) can be expressed as a function of their respective DNs. However, for the case of anions, there is a loss in entropy of the free ions as they join the solvation shell of Li^+ ions. The contribution per ion is given as $(k_B T ln(c_{anion}))$, where c_{anion} is the concentration of the anion. The interactions h_2 and h_3 can thus be expressed as: $h_2 = 0.001844\, DN_{NO_3^-}^2 - 0.11314\, DN_{NO_3^-} - k_B T ln c_{NO_3^-}$, $h_3 = 0.001844\, DN_{TFSI^-}^2 - 0.11314\, DN_{TFSI^-} - k_B T ln c_{TFSI^-}$

The solvent-anion interactions terms represented by (J_{12}, J_{21}, J_{13}, J_{31}) can be modelled in a similar way in terms of the AN of the solvent. We approximate the solvent-anion interactions by assuming that all anions behave similar to the O_2^- anion. The free energy of O_2^- ions, $G_{O_2^-{}_{HA}}$, can be expressed in terms of the half-wave potential of O_2/O_2^- couple in that solvent, U_{O_2/O_2^-}, and then free energy of gas phase oxygen, $G_{O_{2(g)}}$, as:

$$G_{O_2^-{}_{HA}} = G_{O_{2(g)}} + eU_{O_2/O_2^-} \quad (S7)$$

It has been shown experimentally that the half wave potential O_2/O_2^- varies as function of the AN of the solvent.(6) As described in our previous work,(5) the free energy of the anions can be expressed as a function of the solvent's acceptor number to describe the solvent-anion interactions (J_{12}, J_{21}, J_{13}, J_{31}) in our model, and is given as: $J_{12} = -0.00024\, AN_{HA}^2 + 0.029\, AN_{HA}$. The solvent-solvent interaction term (J_{11}) represents the weak van der Waal's forces between the solvent molecules, and is chosen to be -0.01 eV, which lies within the range of values expected for the organic solvents used. The anion-anion coupling term stands for the strong repulsion interactions (J_{22}, J_{23}, J_{32}, J_{33}), and we choose this value to be an order of magnitude higher at 0.1 eV.

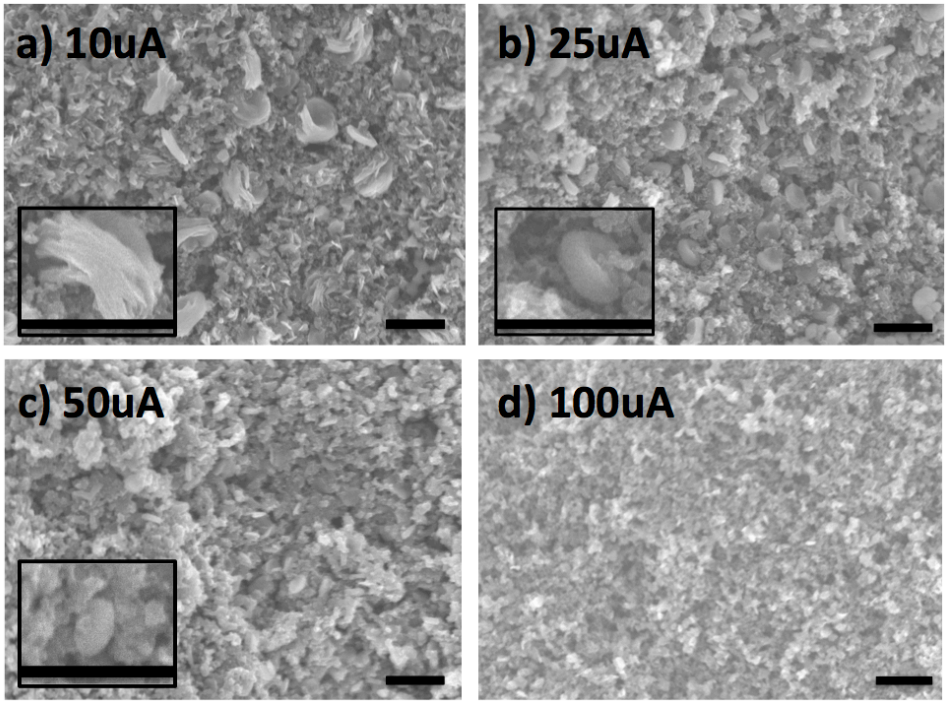

Figure S1. Scanning electron microscope images of carbon cathodes from cells employing 0.5M $LiNO_3$:0.5M LiTFSI in DME discharged to 1mAh capacity at currents of 10μA **(a)**, 25μA **(b)**, 50μA **(c)**, and 100μA **(d)**. Total electrode area was 1.1 cm^2 (12 mm diameter) and typical Vulcan XC72 carbon loading was 1.5-2.0 mg/cm^2.

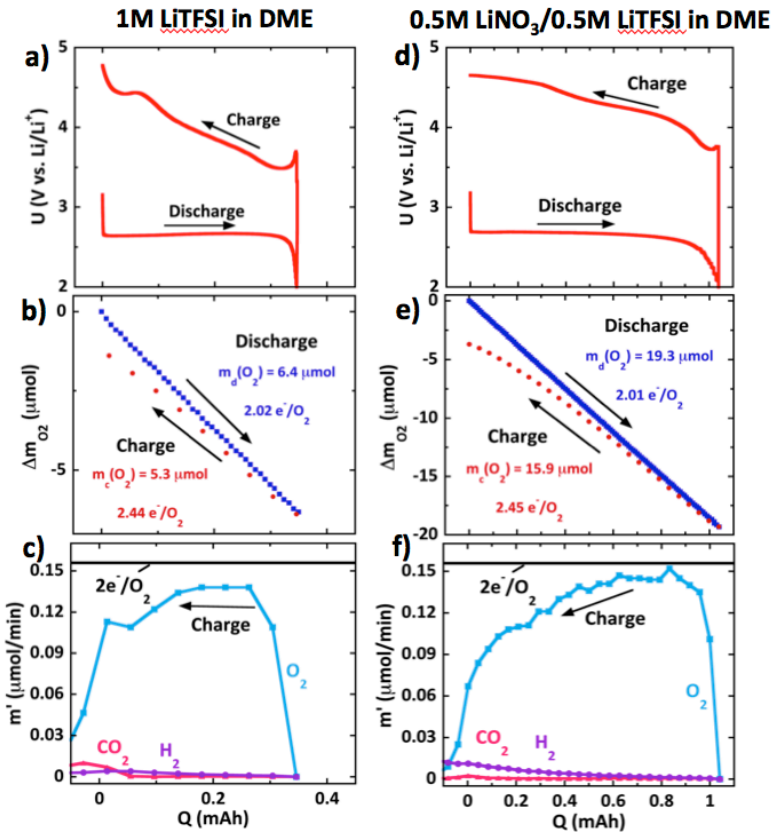

Figure S2. (a, d) Galvanostatic discharge-charge curves for cells employing **(a-c)** 1M LiTFSI in DME and **(d-f)** 0.5M $LiNO_3$:0.5M LiTFSI in DME. **(b, d)** Oxygen consumption during discharge and evolution during charge. **(c, f)** Gas evolution rates for H_2, CO_2, and O_2 during cell charge. These were the only gases found to evolve during charge.

Figures S2(a) and S2(d) present galvanostatic discharge-charge profiles for cells employing 1M LiTFSI and 0.5M $LiNO_3$:0.5M LiTFSI. Discharge, or ORR, overpotentials are similar between the two electrolytes. The cell employing $LiNO_3$ salt, however, exhibited a higher initial charge overpotential, which likely arises from an electronic transport limitation to toroid decomposition, although further studies are necessary to confirm this hypothesis. Figure S6 shows that for cells charged from the same discharge capacity, this initial charge overpotential does increase with increasing $LiNO_3$ concentration. The cause of this trend is currently under investigation.

Figures S2(b) and S2(e) show oxygen consumption as a function of capacity during discharge and charge for these two cells. On both discharge and charge, both cells show nearly identical e^-/O_2, indicating nearly equivalent degrees of

reversibility. Figure S2(c) and S2(f) display gas evolution on charge from DEMS. Oxygen was clearly the dominant gas evolved for both cells, and in nearly identical quantities, with oxygen accounting for 92% of the gases evolved from the 0M $LiNO_3$ (1M LiTFSI) cell, and 93% of the gases from the 0.5M $LiNO_3$ (0.5M LiTFSI) cell. Small quantities of carbon dioxide and hydrogen were evolved from each cell toward the end of charging, with the 0M $LiNO_3$ evolving slightly more carbon dioxide, and the 0.5M $LiNO_3$ cell evolving slightly more hydrogen.

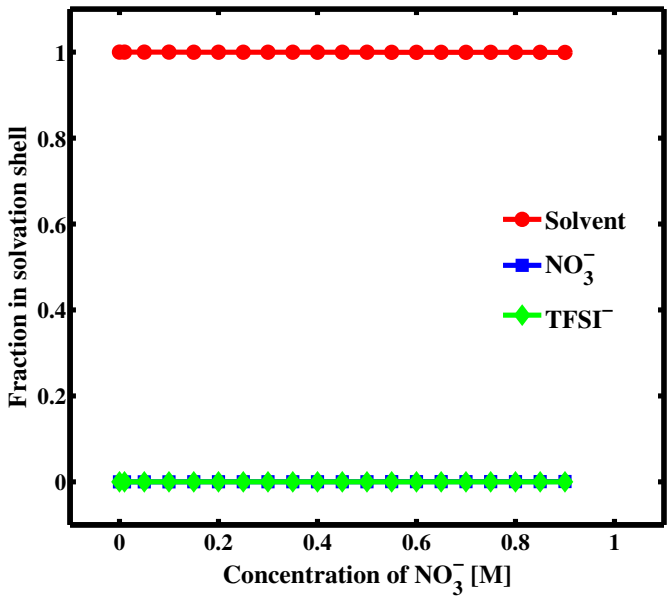

Figure S3. The change in occupation of the solvent DMSO (red line), $TFSI^-$ (green line) and NO_3^- (blue line) in the Li^+ solvation shell as we change the concentration of the NO_3^- anion. $TFSI^-$ and NO_3^- both have lower DNs (11.2 and 22.2 kcal/mol) compared to the solvent DMSO (29.8 kcal/mol). Hence they cannot replace DMSO in the solvation shell. Hence even with increasing NO_3^- concentration, DMSO completely occupies the solvation shell of Li^+.

The occupation variables derived from the model for an electrolyte using DMSO as a solvent is shown in Figure S3. This shows that in DMSO, which is a high-DN solvent, NO_3^- anion is unable to replace DMSO from the solvation shell. The accompanied change in free energy of Li^+ as a function of NO_3^- anion concentration is shown in Figure S4. This shows that there should be almost no change in discharge capacity, consistent with the experiments reported here.

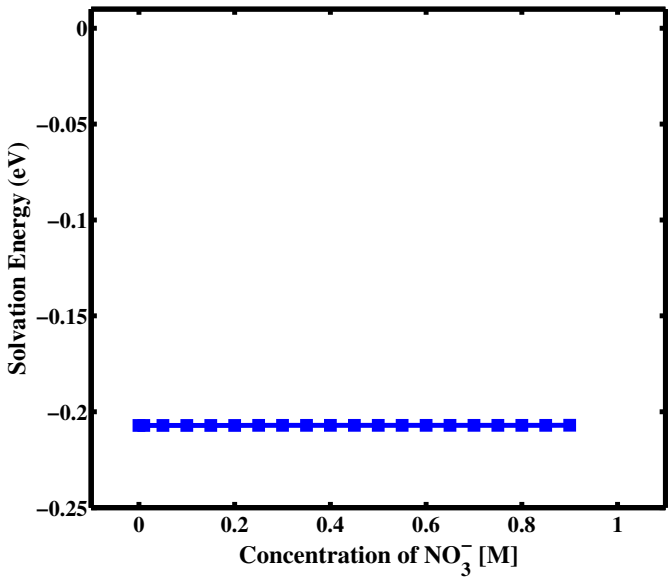

Figure S4. The Li^+ solvation energy (eV) as a function of the concentration of the NO_3^- anion. The solvent used is DMSO and the salt is mixture with different concentrations of $LiNO_3$ and LiTFSI such that the Li^+ concentration is maintained at 1M. The Li^+ free energy of Li^+, calculated relative to DME and 1M LiTFSI, is independent of the NO_3^- concentration when the solvent is DMSO. As a result, the solution rate enhancement is solely due to the high DN solvent DMSO.

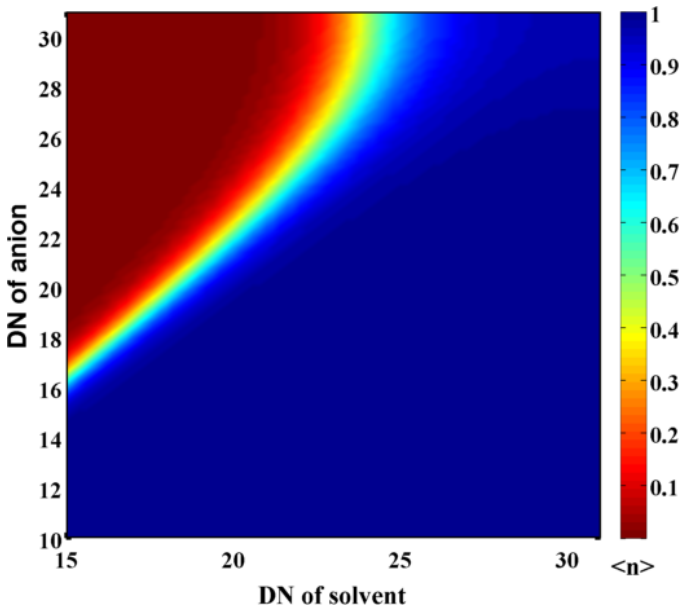

Figure S5. Contour plot showing the occupation in Li^+ solvation shell of the solvent for varying DN (in kcal/mol) of the solvent and salt anion. The salt anions shown are such that they have DN between 10 and 30 while the solvents shown have DN between 15-30. The electrolyte is considered to be a 50:50 mixture of LiTFSI and a salt consisting of Li^+ and the salt anion in the corresponding solvent. The blue region represents high solvent occupation in the Li^+ solvation shell while the red region shows high anion occupation.

Generalized Electrolyte Design

A generalized electrolyte design model is developed based on the Ising model discussed above. A contour map of the occupation of the solvent as a function of varying DN of solvent and anion is shown in Figure S5. This generalized analysis assumes a constant AN chosen to be the average of DME and DMSO and a 50:50 salt blend of LiTFSI and a varying electrolyte anion. The contour map shows that in a low-DN solvent, utilizing a high-DN anion leads to replacement of the solvent by the anion in the solvation shell. For a solvent DN of 20.2 kcal/mol, which corresponds to DME, an anion DN of ~23 kcal/mol leads to an equal amount of solvent and anion in the solvation shell. It is worth highlighting that the occupation is a stronger function of the DN of the solvent than that of the anion. For high-DN (>25 kcal/mol) solvents, the solvation shell is predominatly occupied by the solvent.

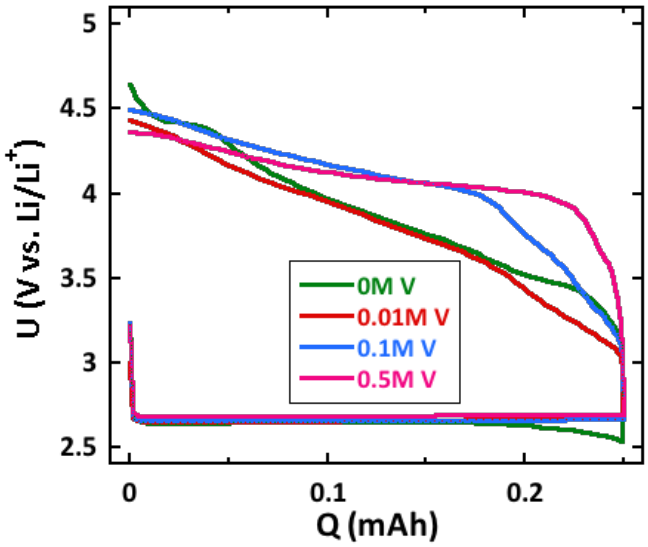

Figure S6. Representative discharge-charge profiles of cells of various $LiNO_3$ concentrations. All cells were discharged at 450 μA/cm^2 to 0.23 mAh/cm^2. A 1.0M Li^+ concentration was used for all cell electrolytes, while the LiTFSI:$LiNO_3$ ratio was varied. The $LiNO_3$ concentration for each cell is provided in the figure legend.

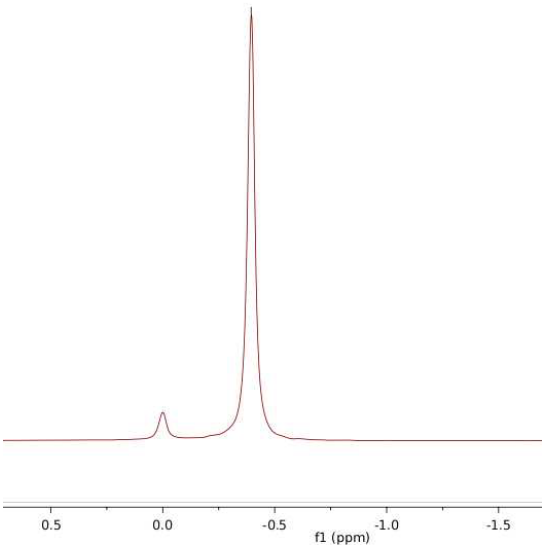

Figure S7. Representative ^{7}Li NMR spectrum on 0.5M LiTFSI/0.5M $LiNO_3$ in DME. The chemical shift at 0 ppm corresponds to the Li shift of LiCl in D_2O, whereas the chemical shift at -0.40 ppm corresponds to the Li shift in the electrolyte.

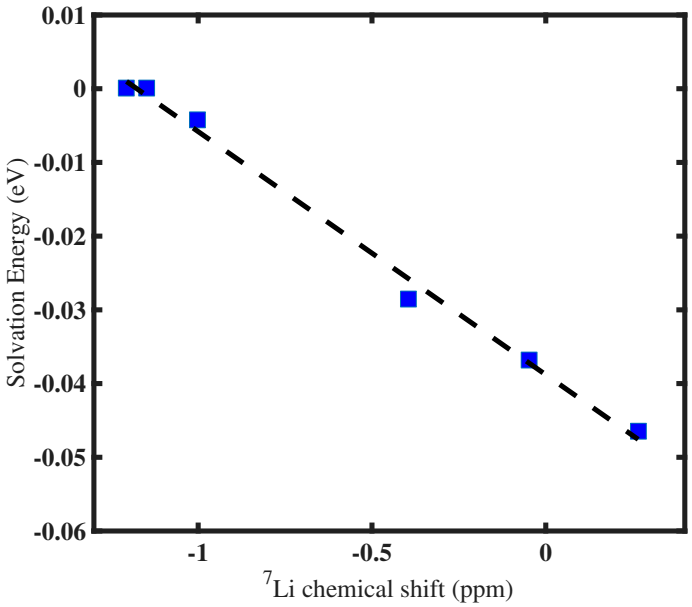

Figure S8. Plot showing the linear correlation between the ^{7}Li chemical shift (ppm) obtained from experiments and the free energy of solvation of Li^{+} (eV) derived from the Ising model when DME is used as the solvent and NO_3^- is used as the salt. The individual points in the plot correspond to different concentrations of $LiNO_3$.

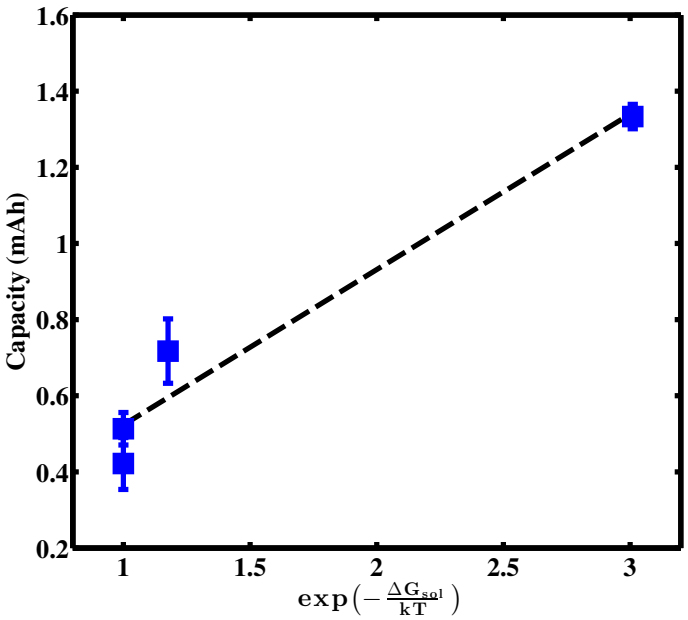

Figure S9. Plot showing the linear correlation between Capacity (mAh) obtained from experiments (from Figure 1a inset) and rate enhancement of the solution process $r_S \sim \exp\left(\frac{-\Delta G_{sol}}{kT}\right)$ as evaluated from the Ising model for various concentrations of $LiNO_3$ in DME. The plot shows that the capacity varies exponentially with the Gibbs free energy of solvation of Li^+ in the electrolyte.

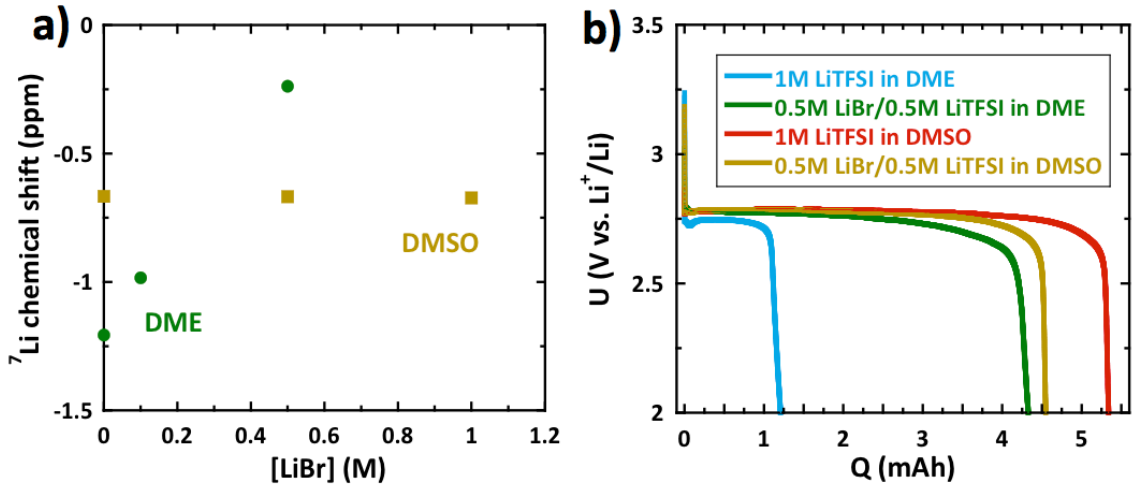

Figure S10. (a) ^{7}Li chemical shift of DMSO and DME-based electrolytes, versus a 3M LiCl in D_2O reference, as a function of LiBr concentration. A less negative chemical shift represents a shift downfield. Analogous to Figure 3a) in the main text, 0.5M Br^- causes a noticeable downfield shift in the ^{7}Li in DME, but not in DMSO. **(b)** Discharge profiles (45μA/cm^2, 1.5 atm O_2 atmosphere, 2V cutoff), as a function of LiBr concentration for both DMSO and DME-based electrolytes. A 1.0 M Li^+ concentration was used for all cell electrolytes, and the LiBr and LiTFSI concentration for each cell is provided in the legend. Analogous to NO_3^- in Figure 3b) in the main text, 0.5M Br^- provides over a three-fold increase in capacity in a DME-based electrolyte, but not in a DMSO-based electrolyte.

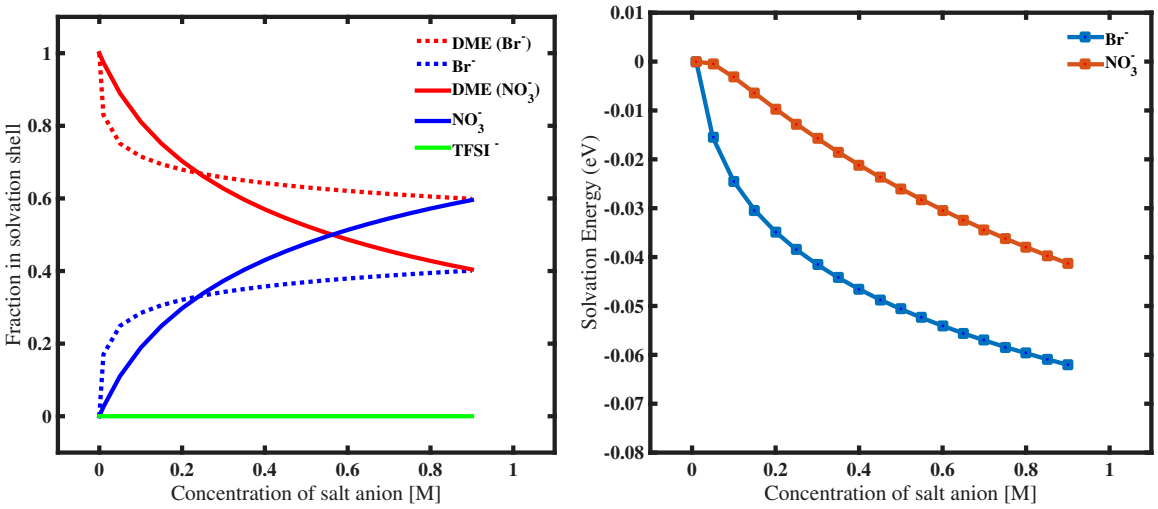

Figure S11. Plots showing the comparison between **(a)** occupations of all species in the solvation shell and **(b)** Li^+ solvation energy as a function of the varied anion concentration (Br^-, NO_3^-) for the two cases: LiBr:LiTFSI and $LiNO_3$:LiTFSI in DME. The electrostatic repulsion terms between the anions (J_{22}, J_{33}, J_{23}, J_{32}) were chosen to be 4 times for the case with Br^- ion compared to the case with NO_3^- ion because $Br^-$is smaller and has a higher charge density.

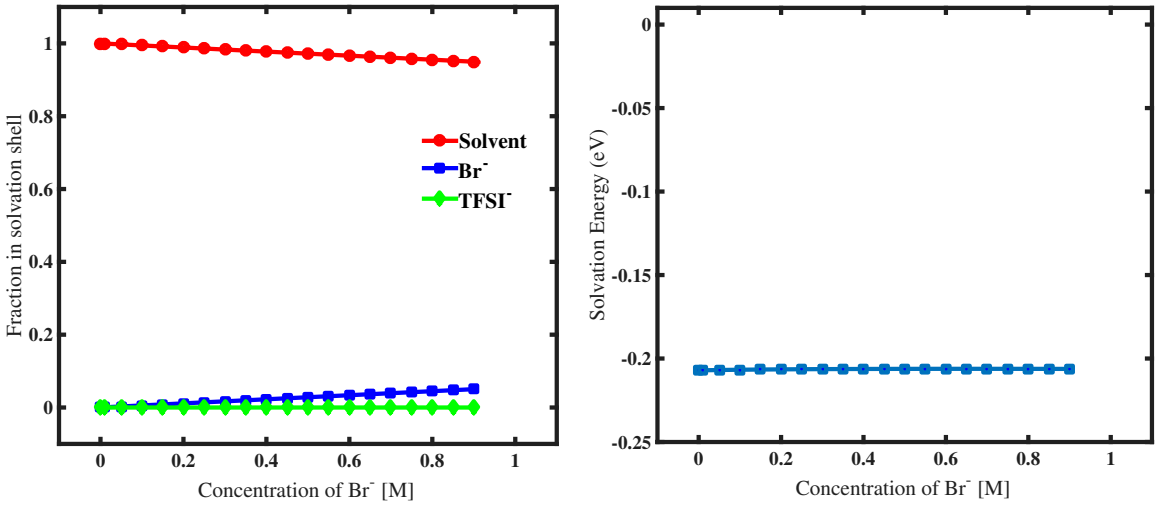

Figure S12. Plots showing the **(a)** occupations of all species in the solvation shell and **(b)** the solvation energy of Li^+ as a function of the Br^- anion concentration for LiBr:LiTFSI as the salt mixture in the solvent DMSO. The Li^+ free energy of Li^+, calculated relative to DME and 1M LiTFSI.

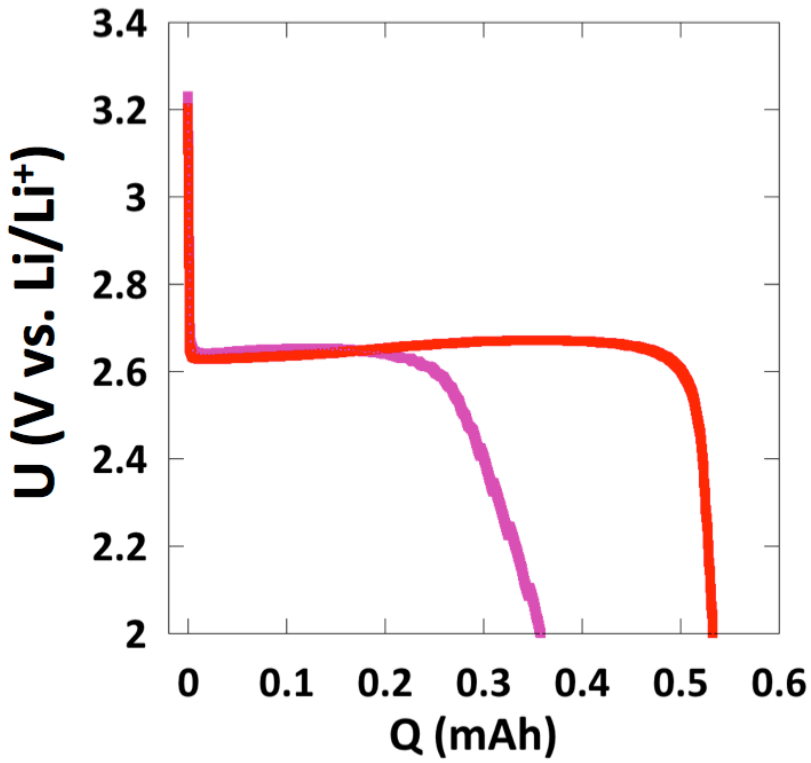

Figure S13. Galvanostatic discharge of a cell employing nominally anhydrous (<10 ppm H_2O, purple curve) and 70 ppm H_2O added (red curve) to 1 M LiTFSI in DME. A small water impurity in the $LiNO_3$ salt led to a linear increase in H_2O content with $LiNO_3$ concentration, with a maximum water content of 70 ppm H_2O in the 0.7N $LiNO_3$ cell. A 40% increase in capacity is observed when 70 ppm H_2O is added to a 1N LiTFSI cell. A greater than 400% increase was observed in the 0.7N $LiNO_3$ cell compared to the anhydrous 1N LiTFSI cell (Figure 1a in the main text).

References

1. McCloskey BD, *et al.* (2013) Combining accurate O_2 and Li_2O_2 assays to separate discharge and charge stability limitations in nonaqueous Li-O_2 batteries. *J. Phys. Chem. Lett.* 4(17):2989- 2993.
2. McCloskey BD, Bethune DS, Shelby RM, Girishkumar G, & Luntz AC (2011) Solvents' critical role in nonaqueous lithium–oxygen battery electrochemistry. *J. Phys. Chem. Lett.* 2(10):1161-1166.
3. Schmeisser M, Illner P, Puchta R, Zahl A, & van Eldik R (2012) Gutmann donor and acceptor numbers for ionic liquids. *Chem. Eur. J.* 18(35):10969-10982.
4. Gritzner G (1986) Solvent effects on half-wave potentials. *J. Phys. Chem.* 90(21):5478-5485.
5. Khetan A, Luntz A, & Viswanathan V (2015) Trade-offs in capacity and rechargeability in nonaqueous Li–O_2 batteries: solution-driven growth versus nucleophilic stability. *J. Phys. Chem. Lett.*:1254-1259.
6. Sawyer DT, Chiericato G, Angelis CT, Nanni EJ, & Tsuchiya T (1982) Effects of media and electrode materials on the electrochemical reduction of dioxygen. *Anal. Chem.* 54(11):1720-1724.